

Magnetic order effects on the electronic structure of $KMMnS_2$ ($M=Cu, Li$) with the $ThCr_2Si_2$ -type structure

Austin Virtue,¹ Xiuquan Zhou,¹ Brandon Wilfong,^{1,2} Jeffrey W. Lynn,³ Keith Taddei,⁴ Peter Zavalij,¹ Limin Wang,² and Efrain E. Rodriguez^{1,2,*}

¹*Department of Chemistry and Biochemistry, University of Maryland, College Park, Maryland 20742, USA*

²*Center for Nanophysics and Advanced Materials, University of Maryland, College Park, Maryland 20742, USA*

³*NIST Center for Neutron Research, National Institute of Standards and Technology, Gaithersburg, Maryland 20899-6102, USA*

⁴*Neutron Scattering Division, Oak Ridge National Laboratory, Oak Ridge, Tennessee 37831, USA*



(Received 22 October 2018; revised manuscript received 6 April 2019; published 30 April 2019)

We study the relationship between antiferromagnetic order and the electronic properties of $KCuMnS_2$ with the $ThCr_2Si_2$ -type structure. We propose two magnetic structures for $KCuMnS_2$ with the $ThCr_2Si_2$ -type structure. Powder samples of $KCuMnS_2$ and $KLiMnS_2$ were prepared for structural studies and magnetization measurements. In both compounds, the Mn^{2+} site is alloyed by either Cu^+ or Li^+ . We also prepared single crystals of $KCuMnS_2$ for x-ray and neutron-diffraction studies and resistivity measurements. We relate these properties to the electronic structure calculated with density functional theory. Neutron-diffraction studies reveal that $KCuMnS_2$ exhibits long-range magnetic ordering with a Néel temperature near 160 K and a moment of $0.92(2) \mu_B/Mn^{2+}$ at 6 K. In contrast, $KLiMnS_2$ never exhibits long-range magnetic ordering down to 3.5 K. Both sulfides never display a crystallographic phase transition from our temperature-dependent x-ray and neutron-diffraction studies. We discuss the magnetic phases in detail and how they relate to isostructural phases such as iron-based superconductors and related chalcogenides. Electrical resistance measurements indicate that while $KCuMnS_2$ is semiconducting, there is an anomaly around the Néel temperature, which indicates that long-range magnetism influences its electronic structure.

DOI: [10.1103/PhysRevMaterials.3.044411](https://doi.org/10.1103/PhysRevMaterials.3.044411)

I. INTRODUCTION

The $ThCr_2Si_2$ -structure type (Fig. 1), also known as the 122-type in the condensed-matter physics literature, represents a large collection of layered compounds that can incorporate much of the periodic table and therefore exhibit a variety of physical phenomena [1,2]. For example, the 122-type pnictides (Pn) and chalcogenides (Ch) with iron have attracted a significant amount of attention because of their superconducting properties. The $BaFe_2As_2$ parent compound can be either aliovalently or isovalently doped to a superconductor from an antiferromagnetic semimetal [3–6]. The structurally related $K_xFe_{2-y}Se_2$ can also express superconductivity, although it is always mixed with an antiferromagnetic, insulating phase due to the distribution of iron vacancies [7–9]. The origin of superconductivity in both pnictides and chalcogenides is still on-going research, and several implied mechanisms including spin fluctuations and nematic electronic states have been proposed [10–14].

Due to the proximity to Fe, we first explore Mn chalcogenides in the 122-type structure to find similar ground states. The ACo_2X_2 series (where $X = Pn$ or Ch and A is an alkali or alkaline-earth metal) tends to express long-range ferromagnetic order [15–18]. For Mn, the magnetism of its 122-type pnictides, such as $BaMn_2As_2$, has been well studied, including by neutron diffraction [19–21]. However, the

ternary 122-type Mn chalcogenides are unknown. Likely, this arises from charge balance arguments. By replacing As^{3-} with Se^{2-} , one must reduce Mn below the +2 oxidation state, which is difficult to do for the stable d^5 transition metal. However, Mn^{2+} can be incorporated into quaternary 122-type chalcogenides by alloying it with a monovalent cation such as Cu^+ or Li^+ [22]. Indeed, $ACuMnCh_2$ and $ALiMnCh_2$ have been reported in the pioneering work of Greenblatt [23–27] and Bronger [28,29], respectively. Unlike the ternary 122-type pnictides, no long-range magnetic ordering was found for $ACuMnCh_2$ compounds in earlier studies [23,24], and no physical property measurements were carried out for $ALiMnCh_2$ [28].

Due to the lack of neutron-diffraction data for these quaternary Mn chalcogenides in previous studies, their underlying magnetic order remains unknown. Hence, more comprehensive studies are needed to elucidate their relationship to structurally related Fe-based superconductors. This is crucial for any attempt to find a new non-Fe-based system that can exhibit superconductivity. We focus here on the sulfides of Mn with the A cation being K^+ . Any future studies on tuning the properties of quaternary Mn sulfides through doping would require an understanding of (1) the underlying magnetic order, (2) the ideal synthetic and crystal growth conditions, and (3) the electronic and transport properties. We therefore reinvestigate and present the preparation, single-crystal growth, chemical and magnetic structures, and ground-state properties of these 122-type quaternary phases.

*efrain@umd.edu

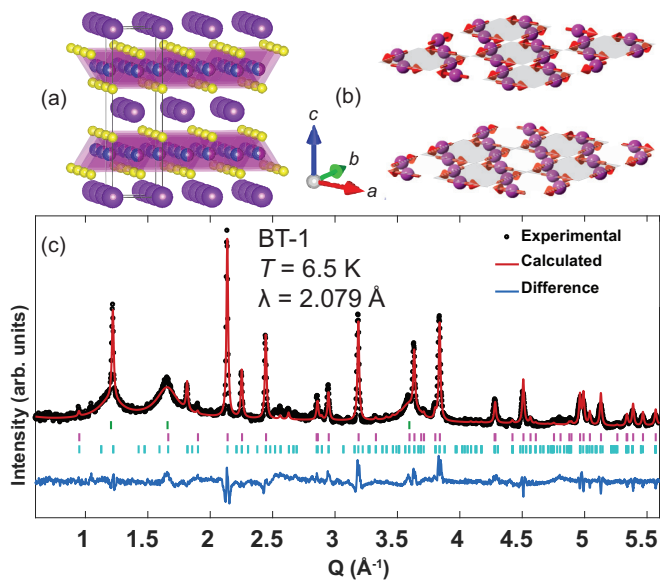


FIG. 1. Chemical and plausible magnetic structure of KCuMnS_2 from neutron powder diffraction. (a) Atomic structure with equal occupancy of Cu/Mn sites (blue and magenta) forming two-dimensional sulfide (yellow) tetrahedral layers separated by potassium (purple) cations. (b) A proposed antiferromagnetic pinwheel magnetic structure of KCuMnS_2 , showing only the magnetic Cu/Mn site, with the moment in the ab plane. This is one of two magnetic structures that fit equally as well to NPD data. (c) Rietveld refinement fit to neutron powder diffraction data ($R_{wp} = 7.211\%$) with magnetic phase (bottom ticks), structural phase (middle ticks), and impurity peaks (top ticks) indicated.

II. EXPERIMENTAL AND COMPUTATIONAL METHODS

The quaternary sulfides were prepared by heating a mixture of pure metals with alkali metal carbonates under a flow of argon charged with carbon disulfide (99.9% ACS reagent grade, Aldrich). Depending on the desired product, stoichiometric amounts of Mn metal (99.95% –325 mesh, Alfa Aesar) were mixed with either Cu metal (99.5% –200 + 325 mesh, CERAC Inc.) or a 5% excess of lithium carbonate (98%, Honeywell) to account for some Li evaporation, along with a 10% excess of potassium carbonate (99% anhydrous, Alfa Aesar). Powders were ground together in an agate mortar and pestle as an acetone slurry to a homogeneous mixture and allowed to dry. A typical synthesis of 12.5 mmol would consist of 0.9502 g K_2CO_3 , 0.4849 g Li_2CO_3 , 0.7943 g Cu, 0.6867 g Mn, and approximately 15 mL of CS_2 .

The mixture was loaded as a powder into an alumina crucible which was then placed into a tube furnace under a flow of argon. The mixed gas flow pathway was set up to flow into and out of a three-neck flask before entering the furnace, exiting the tube furnace through a bleach solution. The furnace was then heated at a rate of 180 °C per hour up to 800 °C. Once the temperature was reached, a 15-fold excess of carbon disulfide was added via syringe to the three-neck flask as a liquid and allowed to evaporate into the argon flow. Following complete evaporation of the carbon disulfide, the sample was cooled to room temperature at 180 °C per hour.

It is important to note that to impede the evolution of toxic H_2S , the end of the CS_2 stream was bubbled through a bleach solution (concentrated Clorox germicidal bleach, active ingredient: 8.25% sodium hypochlorite). The entire apparatus was contained in a fume hood.

The powders that were recovered contained impurities of potassium polysulfide as well as an additional impurity of alabandite for the Li sample. This polysulfide impurity could either be washed away with small amounts of water followed by methanol, or used as the flux for single-crystal growth of the Cu compound, described below.

Single-crystal growth was achieved by placing roughly 0.25 g of the unwashed powder into an evacuated quartz ampule, which was then placed in a second evacuated quartz ampule, heated at a rate of 50 °C per hour to 1000 °C. This temperature was held for 10 hours before cooling at a rate of 6 °C per hour to 500 °C. The ampule was then cooled at a rate of 30 °C per hour to room temperature. Single crystals were then recovered manually.

Neutron powder measurements for KCuMnS_2 were performed on the BT-1 diffractometer at the NIST Center for Neutron Research (NCNR) with wavelength $\lambda = 2.079$ \AA (Ge 311 monochromator) at a base temperature of 6 K. The temperature dependence of the magnetic peak centered at approximately 1.24 \AA⁻¹ was carried out on a single crystal with the position-sensitive detector on the BT-7 triple-axis spectrometer (NCNR) [30] with a wavelength $\lambda = 2.359$ \AA from 10 to 220 K. Neutron powder measurements for KLiMnS_2 were performed on the HB-2A diffractometer at the Oak Ridge National Laboratory, High Flux Isotope Reactor (HFIR), with wavelength $\lambda = 2.4103$ \AA (Ge 113 monochromator). Temperature-dependent powder diffraction patterns were taken starting from a base temperature of 3.5 K. Symmetry analysis was performed using ISODISTORT from the ISOTROPY web-based software suite [31]. Rietveld refinements of the neutron-diffraction data were carried out using the TOPAS 5.0 software [32].

X-ray data were collected on a KCuMnS_2 single crystal of approximate dimensions $0.29 \times 0.13 \times 0.04$ mm in size with Mo $\text{K}\alpha$ radiation of $\lambda = 0.71073$ \AA. The crystal was measured every 20 degrees from 110 to 250 K using the Bruker Smart Apex-II CCD system to uncover any possible crystallographic phase transitions coinciding with the onset of long-range magnetic order. The structure was solved and refined with the SHELX software package [33].

Electrical transport measurements were performed using a 9 T Quantum Design Physical Property Measurement System (PPMS-9) with polycrystalline and single-crystal samples of KCuMnS_2 . Polycrystalline samples were ground into a powder and pressed into pellets utilizing < 2 ton uniaxial load without sintering. Electrical resistivity was measured using the four-probe method with gold wire and contacts made with silver paste. The temperature and field dependence of longitudinal electrical resistivity were measured in a range from 300 to 1.8 K with applied current of 0.1 mA and frequencies near 17 Hz.

Temperature-dependent dc (direct current) magnetic susceptibility measurements were carried out using a Quantum Design Magnetic Property Measurement System (MPMS) on powder samples of KCuMnS_2 and KLiMnS_2 . Field-cooled

TABLE I. Single-crystal x-ray diffraction data for KCuMnS_2 .

Space group	$I4/mmm$ (No. 139)
a (Å)	3.9442(8)
c (Å)	13.239(3)
Crystal system	Tetragonal
Volume (Å ³)	205.96(9)
Z	2
Calculated density (g cm ⁻³)	3.575
λ , Mo $K\alpha$ Å	0.71073
No. reflections collected	1080
No. independent reflections	133
$F(000)$	210.0
R_1, wR_2 (%)	2.01, 4.31
Temperature	110 K

(FC) and zero-field-cooled (ZFC) measurements were taken from 1.8 to 300 K with an applied magnetic field of 500 Oe. Magnetization versus field loops were carried out using the MPMS from -7 to 7 T on the powder samples at 2 and 50 K.

The initial density functional theory (DFT) [34,35] calculations for a simple layered Néel-type magnetic structure were performed by using the Vienna *Ab initio* Simulation Package (VASP) [36–39] software with potentials using the projector-augmented wave (PAW) [40] method. The exchange and correlation functional was treated by the Perdew-Burke-Ernzerhof generalized gradient approximation (PBE-GGA) [41]. The cutoff energy, 450 eV, was applied to the valence electronic wave functions expanded in a plane-wave basis set for all chalcogenides. A Monkhorst-Pack [42] generated $21 \times 21 \times 7$ k -point grid was used for the Brillouin-zone integration to obtain accurate electronic structures.

In order to demonstrate the effects of the antiferromagnetic (AFM) order on the electronic structure for KCuMnS_2 , the nonmagnetic and magnetic DFT calculations are conducted using VASP with the projector-augmented wave basis in the generalized gradient approximation. The enlarged 2×2 magnetic unit cells are shown in Fig. S2 of the Supplemental Material [43], which correspond to the stripelike and noncollinear AFM order suggested by our neutron experiment. The cutoff energy, 450 eV, was applied and the γ -centered k mesh was taken to be $9 \times 9 \times 7$ and $21 \times 21 \times 7$ for the magnetic and nonmagnetic cases, respectively.

III. RESULTS

A. Crystal structure

Details of the x-ray measurement results on the KCuMnS_2 single crystal are gathered in Table I, which shows that the sample crystallizes in a body-centered tetragonal crystal system. The lattice constants are $a = 3.9442(8)$ Å and $c = 13.239(3)$ Å at 110 K in space group $I4/mmm$ (No. 139). Structural parameters are presented in Table II. All occupancies are refined to unity. The Cu and Mn atoms share half of the $4d$ Wyckoff position, which has a site symmetry of $-4m2$. No superlattice reflections that would imply any ordering of the Mn and Cu atoms on the $4d$ site were observed. The crystal was found to retain tetragonal symmetry at all temperatures measured. The temperature dependence of the

TABLE II. Structural, lattice, and anisotropic displacement parameters for $I4/mmm$ KCuMnS_2 from single-crystal data at 110 K. All off-diagonal terms are equal to zero.

Atom	Wyckoff site	x	y	z	U_{ij} (Å ²) = U_{22}	
					(Å ²)	(Å ²)
K	2a	0	0	0.5	0.0118(4)	0.0158(7)
Cu/Mn	4d	0.5	0	0.75	0.0071(2)	0.0153(3)
S	4e	0.5	0.5	0.35607(9)	0.0071(3)	0.0121(5)

lattice parameters from single-crystal data did not reveal any structural anomaly from 110 to 250 K (see Fig. S1 in the Supplemental Material [43]).

The structure obtained from the single-crystal x-ray results (Tables I and II) was used to model and fit the neutron powder diffraction (NPD) data. The NPD pattern revealed extra reflections at base temperature, which we attribute to antiferromagnetic ordering. These satellite reflections were indexed with a propagation vector of $\mathbf{k} = (\frac{1}{2}, \frac{1}{2}, 1)$, and are discussed in the next section.

The KCuMnS_2 neutron powder sample contained an unknown impurity causing three broad background peaks in the BT-1 data. Likely, the impurity in the powder sample is either a poorly crystallized sulfide or elemental sulfur that could not be washed away. These broad, and likely amorphous peaks were fit with three Gaussian peak profiles that may be attributed to the same impurity as they all possessed the same peak profile parameters. Refinement of the structural model shown in Fig. 1(c) with an $R_{wp} = 7.211\%$ indicates full occupancy of all sites in the structure. From NPD, the lattice constants were refined to $a = 3.9405(2)$ Å, $c = 13.215(1)$ Å at 6 K. From temperature-dependent NPD measurements, we did not detect any break of the tetragonal symmetry.

Changing the monovalent cation from Cu to Li subtly effects the crystal structure as obtained from Rietveld refinement with the NPD data at 3.5 K (Fig. 2). The compound retains the tetragonal structure but the a parameter length-

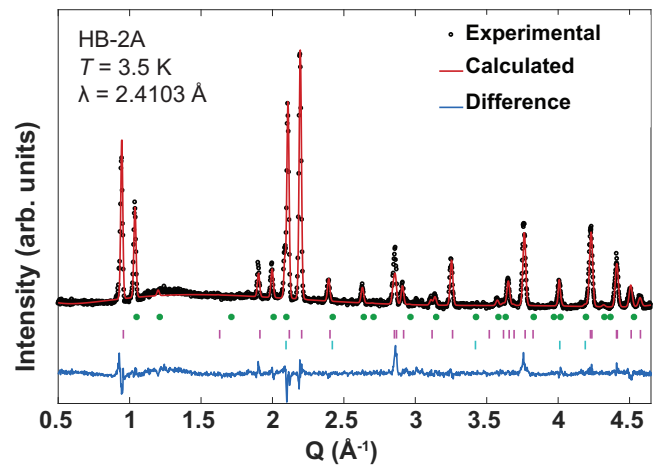


FIG. 2. Rietveld refinement of the structure of KLiMnS_2 with neutron-diffraction powder diffraction data at 3.5 K, $R_{wp} = 7.019\%$. Top tick marks are for KLiMnS_2 and bottom tick marks are for the MnS alabandite impurity, with its magnetic peaks indicated by circles.

ens to 4.0312(2) Å [from 3.9405(2) Å in Cu], while the c parameter contracts to 13.1453(8) Å. Using isotopically pure ^7Li , the NPD is fit nicely with the 122 structure along with a <5 wt.% MnS alabandite impurity. At 200 K, without the additional magnetic peaks to index, the occupancy of the $4d$ site refines to 0.489(6) with Mn and 0.48(1) with Li, leading to a site roughly that is 97% occupied. Likely, the loss of Li from evaporation leads to the alabandite impurity. Nevertheless, increasing the initial amounts of Li carbonate did not diminish the amount of alabandite impurity.

B. Magnetism and magnetic structure

First, we report the results from the magnetization measurements. For both powder and single-crystal samples of KCuMnS_2 , the magnetic susceptibilities display similar features. The susceptibility in Fig. 3(a) decreases as the temperature is lowered and no clear cusp in the curve is observed down to 2 K. At 40 K, a Curie tail appears. However, the derivative of the fits to both the zero-field-cooled (ZFC) and field-cooled (FC) curves reveals a subtle feature near 160 K. When fit to a polynomial between 100 and 250 K, the first derivative [Fig. 3(a) inset] of the temperature-dependent magnetic susceptibility remained fairly constant (above 40 K). Therefore, it is likely that the system displays some low-dimensional magnetic coupling or competition between multiple magnetic structures that almost completely flatten the cusp-type feature typical of three-dimensional (3D) antiferromagnets [44–47].

In order to elucidate any possible magnetic ordering in KCuMnS_2 , we performed temperature-dependent NPD and single-crystal neutron diffraction (BT-7). As shown in Fig. 4, the onset of long-range order occurs around 160 K from the magnetic peak centered around 1.24 \AA^{-1} . The peak was fit to a Gaussian, and the parameters of the profile shape were analyzed as a function of temperature. The integrated intensity (I) vs T is shown in the inset of Fig. 4. Fitting the order parameter of magnetization M , which scales with \sqrt{I} , yielded a Néel temperature $T_N = 160.5(1) \text{ K}$ and a critical exponent of $\beta = 0.334(3)$, which is close to the β of a 3D Ising system (0.3264).

From the propagation vector of $\mathbf{k} = (\frac{1}{2}, \frac{1}{2}, 1)$, three plausible space groups for the antiferromagnetic order were proposed. First, the so-called striped phase is presented in Fig. 5. Here, the moments on the Mn^{+2} ions align in a stripe pattern with alternating layers oriented antiferromagnetically. This magnetic structure can be fit with magnetic space group C_A/mmm (65.489). A view of the magnetic moments and Mn sites from the c axis (Fig. 5) shows that the magnetic unit cell (blue solid line) can be thought of as a $2a \times 2a$ cell of the chemical unit cell (green short-dashed line). A further simplified magnetic cell can be adjusted to a $\sqrt{2}a \times \sqrt{2}a$ cell, which then has the symmetry of magnetic space group C_A/mmm .

The other two possible magnetic symmetries are non-collinear ones and are presented in Fig. 6. Interestingly, these two models give an identical fit to the NPD data to that of the striped phase. Magnetic space groups P_C4mmm (123.349) and P_Cmmm (47.255) retain the same unit cell ($\sqrt{2}a \times \sqrt{2}a$) as the proposed C_A/mmm structure detailed above, but lead to a noncollinear arrangement of the moments. The structures

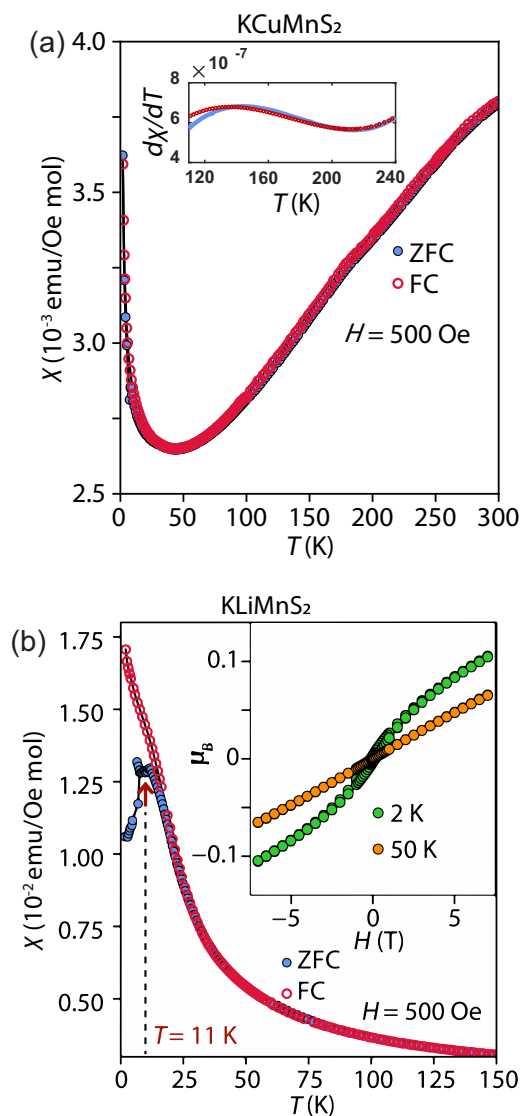


FIG. 3. Temperature-dependent magnetic susceptibility of (a) KCuMnS_2 and (b) KLiMnS_2 . The inset of (a) is the derivative of the susceptibility and shows a subtle feature around the Néel temperature of 160 K. [Conversion to SI units: 1 Oe = $(1000/4\pi) \text{ A/m}$, $1 \text{ emu}/(\text{mol Oe}) = 4\pi \cdot 10^{-6} \text{ m}^3/\text{mol}$].

for P_C4mmm and P_Cmmm provide identically good fits to the NPD data, which is to be expected as they are ultimately the same magnetic structure displaced by $\frac{a}{2} + \frac{a}{2}$. However, P_C4mmm does preserve fourfold symmetry within the unit cell, whereas the other does not. As with the striped structure, the magnetic moments of the Mn cations lie only in the ab plane and are antiferromagnetically coupled between the alternating layers (i.e., along the c axis), as shown in Fig. 1(b). When comparing the two possible magnetic structures to one another, it is important to recall that the occupancy of the magnetic site is only half Mn, with no evidence of long-range ordering of Mn and Cu cations.

Since the system remains tetragonal below the magnetic transition temperature, we can only measure the directional cosine angle of the magnetic moment with respect to the ab plane. For all three models, however, the moment is only

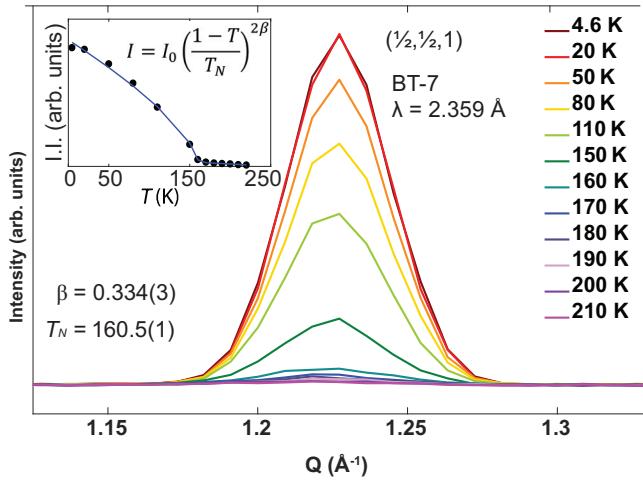


FIG. 4. Temperature dependence of a magnetic Bragg peak in a single-crystal sample of KCuMnS_2 from neutron diffraction. Inset: The integrated intensity of the peak is plotted vs temperature in order to fit the magnetic order parameter. From the least-squares fit, we extract a Néel temperature close to $160.5(1)$ K and a critical exponent β of $0.334(3)$.

along the ab plane. At 3.5 K, the moment size refined to $0.462(9) \mu_B$ for the Cu/Mn site. Given that Cu^+ is a d^{10} cation, we can infer that the moment is solely from the Mn cation. Attributing for the occupancy of the site, the moment therefore refines to $0.92(2) \mu_B/\text{Mn}^{2+}$. This moment size is still approximately 20% of that anticipated for a d^5 cation.

Upon changing the monovalent cation, the magnetic properties are dramatically altered. At low-temperature patterns of the NPD data in Fig. 2, strong magnetic peaks were observed; however, none of these actually belonged to KLiMnS_2 . All could be successfully attributed to the magnetic peaks from the alabandite rock-salt cubic structure, which is well known for both MnS and MnO [48–52]. A broad hump that appears centered around 1.25 \AA^{-1} could indicate some short-range ordering with a lack of long-range ordering of the magnetic moments. However, this extra scattering could also arise

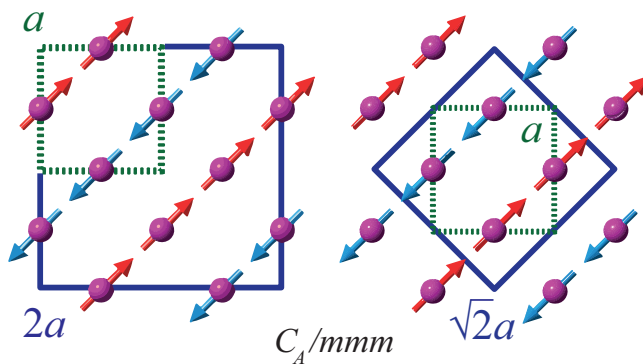


FIG. 5. Proposed striped phase, C_A/mmm magnetic structure of KCuMnS_2 with Mn atoms. The structural lattice is shown with a green short-dashed line; the magnetic cell is shown as both the $2a \times 2a$ (left) and the $\sqrt{2}a \times \sqrt{2}a$ (right) of the structural cell with a blue solid line.

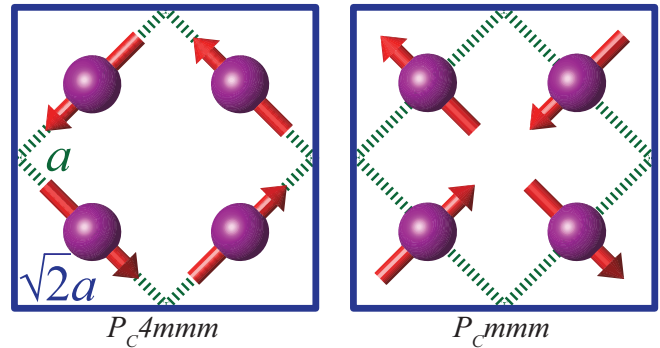


FIG. 6. Alternate noncollinear magnetic phases for KCuMnS_2 . The P_C4mmm (left) phase and the P_Cmmm (right) magnetic structure of KCuMnS_2 with Mn atoms. The structural lattice is shown with a green dashed line; the magnetic cell is shown with a blue solid line (rotated 45° from Fig. 5).

from inelastic scattering and we cannot therefore definitively assign it to a spin-glassy state in KLiMnS_2 . Although powder samples of KLiMnS_2 [Fig. 3(b)] show a cusp in the magnetic susceptibility below 11 K, this may not lead to long-range order as evidenced by the NPD data. The known Néel temperature for the alabandite found in NPD occurs at approximately 75 K [48], which rules out this 11 K feature as arising from impurity.

C. Electrical resistivity and electronic structure

Measurements for the resistance of a pressed pellet and resistivity along the ab plane of a single crystal of KCuMnS_2 are presented in Fig. 7. Both samples show primarily semiconducting behavior with a distinct transition near 150 K. Below this transition, both samples exhibit metalliclike

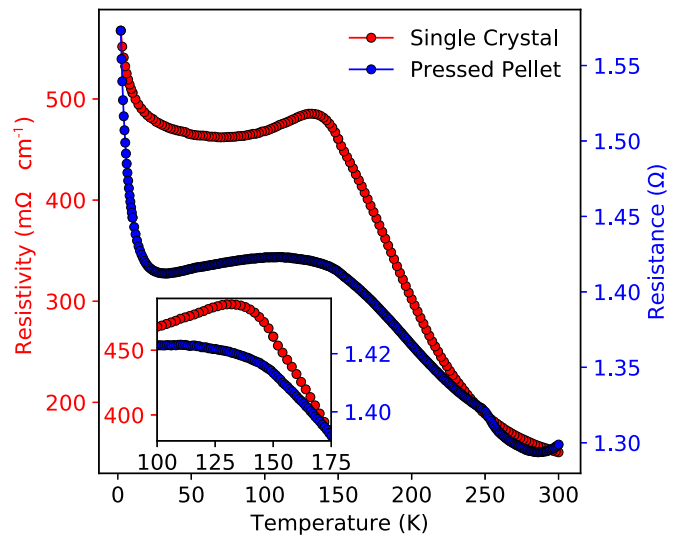


FIG. 7. Temperature-dependent resistance of KCuMnS_2 pressed pellet (blue, bottom), and resistivity for a single crystal of KCuMnS_2 along the ab plane (red, top). Semiconductor-to-metallic behavior is observed below 150 K, which is proximate to the onset of long-range magnetic ordering (approximately 160 K), before resuming semiconductor behavior.

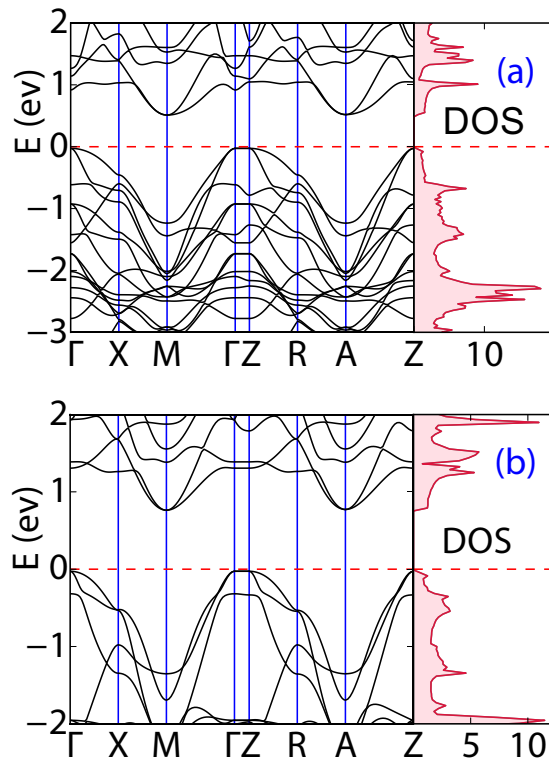


FIG. 8. Dispersion curves and DOS of the electronic states near the Fermi level for (a) KCuMnS_2 and (b) KLiMnS_2 showing the Fermi level on the edge of the valence band.

behavior since the resistance (resistivity) of both decreases with temperature until semiconductor behavior resumes at lower temperatures. For the polycrystalline sample, this occurs near 30 K, and for the single crystal near 80 K. The anomaly in the transport results is more distinct in the single-crystal sample (Fig. 7 inset), which likely arises from powder averaging, although the transition at lower temperature is more distinct in the pressed-pellet sample.

The anomaly in the resistivity of the KCuMnS_2 single crystal occurs near the Néel temperature of 160 K, indicating that long-range magnetic order leads to an increase in the conductivity of the sample. This is further supported by the lower-temperature transition prominent in the powder sample which resumes semiconductor behavior around 30 K at the same time as the magnetic intensity from Fig. 4 begins to saturate. We were not able to measure the resistivity along the c axis for the single-crystal sample of KCuMnS_2 due to the sample morphology and were unable to obtain consistent results for KLiMnS_2 samples.

Density functional theory (DFT) calculations were also performed for both KCuMnS_2 and KLiMnS_2 to help gain a better understanding of the electrical transport properties. The dispersion curve of the electronic states near the Fermi level along major symmetry directions and density of state (DOS) from DFT for the simple layered checkerboard Néel-type magnetic structure in Fig. S2 (see Supplemental Material [43]) can be seen in Fig. 8 for both compounds. Unsurprisingly, given that all the cations have either full or half-full shells, the electronic DOS shows both to be semiconductors

with band gaps near 0.5 eV for KCuMnS_2 and 0.8 eV for KLiMnS_2 . Since the Fermi level is on the edge of the valence band for both compounds, these materials would be more susceptible to hole doping to tune the electronic properties.

IV. DISCUSSION

A. Structure and bonding

With both sulfides crystallizing in the $I4/mmm$ space group, the only refinable structural parameter is the z position for the $4e$ site of the sulfide anion. The effective ionic radii of Li^+ (0.59 Å) and Cu^+ (0.60 Å) [53] are very similar, yet the nature of the monovalent cation greatly affects the z position of the sulfide anions and cell parameters. The S-M-S tetrahedral bond angles better illustrate this drastic change. While the CuS_4 tetrahedron has nearly ideal values of $109.22(4)^\circ$ and $109.60(2)^\circ$ for the S-M-S bond angles (from single-crystal XRD at 250 K), the LiS_4 tetrahedron has bond angles of $112.6(2)^\circ$ and $107.94(8)^\circ$ (from NPD data at 200 K). Therefore, the ionic radii do not play a role in determining the key structural parameter in this system, but rather the electronics may be playing the larger role. A full $3d^{10}$ shell as opposed to a full $1s^2$ shell could more effectively hybridize with the sulfur $3p$ levels due to better matching of the orbital energy levels.

Because of the symmetry constraints of the crystal system, there is only one unique M-S bond distance in this system. Interestingly, while the S-M-S bond angles were drastically changed by the nature of M , the bond distance is unaffected. In KMMnS_2 , the M-S interatomic distance is given by $2.4270(7)$ Å and $2.431(2)$ Å for $M = \text{Cu}$ and Li , respectively. These distances are close to that of $2.439(3)$ Å reported by Bronger *et al.* [28]. Nevertheless, the change in the S-M-S bond angle causes an increase of the a parameter and decrease of the c parameter for $M = \text{Li}$ with respect to $M = \text{Cu}$. This is due to the fact that the tetrahedral angle within the ab plane increases, while that out of the plane decreases.

We conclude that the relevant structural changes from diffraction patterns demonstrate that ionic radii are not the only determining factor in these quaternary sulfides. The nature of M is quite important due to the orbitals that are engaged in bonding. The nearly ideal tetrahedron created by the Cu^+ will constrain the magnetic Mn^{2+} , while this is not the case for Li^+ . Covalent bonding is strengthened between metal and sulfur for the case of $M = \text{Cu}^+$. Undoubtedly, this will have an effect on the crystal-field splitting energies for the d^5 cations and the electronic structure, which we discuss next.

B. Electrical transport and sample preparation

Although transport measurements indicate that both sulfides are semiconducting, only the $M = \text{Cu}$ sample displayed a sufficiently small band gap to measure resistivity down to base temperature. It is apparent in the temperature dependence of the single-crystal sample of KCuMnS_2 that the anomaly in the resistivity is related to the antiferromagnetic transition. A similar anomaly has been found in the parent superconductor Fe_{1+x}Te for $x = 12\%$, whereby the T_N causes an anomaly in the semiconductor-type resistivity measurement [54–59].

This has been attributed to scattering from spin fluctuations that persist below the ordering temperature, and a similar phenomenon may be occurring with KCuMnS_2 .

The predicted band gaps in KCuMnS_2 and KLiMnS_2 are 0.5 and 0.8 eV, respectively. Likely, the nearly ideal tetrahedral environment in KCuMnS_2 causes more orbital overlap between the Cu/Mn metal and S anions, thereby increasing the bandwidth of the conduction band. Another notable difference in the calculated band structure is that the Cu d states create more electronic states between 0 and -2 eV as evidenced by the dispersion curves in Fig. 8. Therefore, a distribution of electronic DOS near the Fermi level is created by these extra states in the Cu compound.

The similarity of our KCuMnS_2 structure with that reported by Oledzka is in contrast with the noticeable differences between the resistivity measurements reported here and those of Oledzka *et al.* [23]. The previous results by Oledzka are consistent with that of a highly doped or degenerate semiconductor, with metallic behavior above 80 K, but with resistances too high to be called metallic. While the magnitude of the resistivity for each report is relatively consistent, even with the differences between how the samples were prepared for measurement (sintered vs pressed pellet and single crystal), our results are more in line with the ACuCoS_2 semiconductors also prepared by Oledzka *et al.* [26]. Apart from the reduction in resistivity during the onset of the magnetic moment, not seen in ACuCoS_2 , our resistivity measurements show semiconducting behavior.

The difference in the resistivity measurements between the two reports for KCuMnS_2 can be explained by the seemingly trivial differences between our synthesis and that of previous work. In Ref. [23], the as-recovered powders were washed with water, whereas we washed the excess flux with methanol. Washing with water could have removed some of the K^+ ions in the structure, as can readily happen with other known 122-type chalcogenides such as KCo_2Se_2 [60]. Removal of K^+ from the lattice would oxidize the metal and therefore effectively hole dope the system. With sufficient lowering of the Fermi level into the valence band, the compound may express metallic behavior. This semiconducting behavior is also present in the ACuFeS_2 compounds by Oledzka, though the values for resistivity were too great to measure below 200 K. The deviation from the predicted metallic behavior from electronic band calculations are partially explained by a nonideal tetrahedral environment for the Cu/Fe site.

C. Comparison of AFM models

Although we could not determine the definitive antiferromagnetic structure of KCuMnS_2 from neutron diffraction, other evidence may point in favor of one structure over the other. First, the stripe order would break fourfold symmetry in the compound, as often happens with the 122-type iron arsenides [61]. In those parent phases of the superconductors, the T_N is either coincident or near a tetragonal-to-orthorhombic phase transition [62–66]. Likewise, the Fe_{1+x}Te system displays a structural phase transition near the Néel temperature. The above-mentioned compounds all display either single-stripe or double-stripe antiferromagnetic order [55,56]. However, this phase transition is clearly not the case

in the quaternary 122-sulfides studied here. The lack of a structural transition upon AFM order strengthens the case for the noncollinear structure. The critical exponent of $\beta = 0.331(5)$ for the magnetization from the neutron measurements is closest to the value found for an Ising spin system in a three-dimensional (3D) lattice. A similar noncollinear structure was determined for the Mott insulator $\text{La}_2\text{O}_2\text{Fe}_2\text{OSe}_2$, which was found to be a 2D Ising system [67].

Clearly, some AFM order is needed to explain the semiconducting behavior, and the DFT results offer guidance on the true state in the KCuMnS_2 system. The band structure and DOS in Fig. S3 (see Supplemental Material [43]) predict KCuMnS_2 to be metallic if AFM order is excluded. The AFM model (layered checkerboard) led to the electronic DOS of Fig. 8, which shows KCuMnS_2 to be semiconducting. While simple to construct, this model is obviously wrong according to the neutron-diffraction results. Therefore, we performed additional band structure calculations in order to understand how other magnetic structures may influence the electric properties. We constructed two additional AFM models. One model has the Cu and Mn cations ordered in a double-stripped fashion in order to construct the striped AFM order on the Mn site. The other model has Mn arranged so that it forms a tetramer that would support the noncollinear AFM models of Fig. 6. Both models have a 2×2 magnetic unit cell and are illustrated in Fig. S2 (see Supplemental Material [43]).

In the case of KCuMnS_2 , the two types of AFM order (striped and noncollinear) do not lead to qualitatively different electric properties from each other. However, their electronic DOS are quite different. As shown in the DOS of Fig. S3 (see Supplemental Material [43]), for the striped model, it appears that KCuMnS_2 is not quite a semiconductor but instead a metal with a very small Fermi surface. The Fermi level just crosses the top of the valence band. In the noncollinear AFM model, the same is true but there are some extra states near the valence band that would suggest a smaller band gap if it was a semiconductor. The total energies from the band structure calculations are presented in Table S1 (see Supplemental Material [43]), which shows the striped order to be the lowest energy of all the AFM models. We must be careful in over interpreting these results, however, in that the Cu and Mn cations always remain disordered in KCuMnS_2 and the DFT results only reflect the case for particular types of cation ordering. From these limited calculations, however, the striped order would seem to be favored.

Determination of the correct magnetic structure could be aided by future experiments on the system. The most straightforward approach would be single-crystal transport measurements such as angle-dependent magnetoresistance and/or angle-dependent magnetization measurements. Furthermore, a comprehensive way to understand the structure would be polarized single crystal or powder neutron diffraction, which would definitively allow for the magnetic structure to be solved.

D. Comparison with other 122 systems

Once again, it is interesting to compare the results here to those found previously on KCuMnS_2 . Oledzka *et al.* observed a broad plateau just below room temperature for KCuMnS_2 ,

which is attributed to short-range antiferromagnetic behavior [23]. They proposed that the suppression of magnetic ordering was due to the disruption caused by the Cu^+ ions in the square lattice, even though there may be strong antiferromagnetic exchange between the Mn^{2+} ions. However, we did not find such a divergence between the ZFC and FC curves in our magnetic susceptibility measurements. Again, this may be due to how we processed the sample after synthesis and the spin-glassy behavior may arrive from vacancies rather than the random distribution of Cu^+ cations. The random distribution of the M cations in the structure leading to clusters of Mn^{2+} is also noted as the cause for the reported divergence between ZFC and FC below 38 K, and attributed to a spin-glassy transition [23]. However, such divergence was absent from our current measurements with the KCuMnS_2 system, suggesting lack of the spin-glass phase.

We also consider the closely related KCuFeS_2 and KCuCoS_2 , which are isostructural. Oledzka found KCuFeS_2 to also be an antiferromagnet with a T_N of 40 K, although no neutron diffraction was ever carried out to investigate the possible order [23]. While a split in their ZFC and FC curves at low temperatures may suggest some spin glassiness from the random distributions of Fe and Cu cations, this explanation would not be consistent with the case of KCuCoS_2 . In this compound, the Co and Cu cations are also randomly distributed, yet the system undergoes a ferromagnetic transition near 120 K [26].

Spin-glass behavior is not common for most of these 122-type quaternaries. For KCuCoS_2 , despite having the same random orientation of magnetic ions, the d^8 Co instead undergoes a ferromagnetic transition around 120 K. In the case of KCuCoS_2 , it is believed that c -axis interactions dominate above the T_c , while ab -plane interactions make the overall order ferromagnetic below the T_c . This T_c can change due to the temperature of synthetic conditions similar to ours, dropping drastically to 50 K when the reaction temperature is increased from 720 to 900 °C possibly attributed to changes in the Co/Cu distribution, or sulfur vacancies.

Spin-glass behavior is also not observed in the AMn_2Pn_2 compounds that exhibit antiferromagnetic behavior, possibly higher than room temperature [44,68–70]. Their G-type order indicates Mn^{2+} in the high-spin tetrahedral coordination. This is in contrast to our NPD providing a $0.92(2) \mu_B/\text{Mn}^{2+}$, which indicates low-spin Mn^{2+} in a tetrahedral environment. Indeed, this leads our results to more similarly resemble the class of isostructural AMn_2Pn_2 compounds. BaMn_2Sb_2 and BaMn_2As_2 have both shown themselves to be G-type collinear antiferromagnets, with no c component to the magnetic moment [44,68]. The magnetic susceptibility can also be highly anisotropic with respect to the ab plane for these AMn_2Pn_2 compounds, demonstrating a clear feature in the susceptibility at the Néel temperature when measured parallel to the c axis, that is much less pronounced when measured in the ab plane [44,47]. A strong dominating ab -plane contribution to the magnetic susceptibility could contribute to the presence of only a subtle feature in our powder samples.

The notable difference here is that while BaMn_2Sb_2 has a T_N of 118 K, the T_N of BaMn_2As_2 is well above room temperature at 625 K [69]. While the magnitude of the magnetic moments for the AMn_2Pn_2 compounds is less than

the nominal $5.0 \mu_B/\text{Mn}$ for high-spin Mn^{2+} , the values of roughly $3.75 \mu_B/\text{Mn}$ are still well above that for KCuMnS_2 [45,71–74]. While this decrease for the pnictides is attributed to the strong spin-dependent hybridization of the Mn $3d$ and As $4p$ orbitals, the reduction for KCuMnS_2 is likely similar to that of the Fe-122 compounds due to the itinerant nature of the magnetism. It is this itinerant nature that could help KCuMnS_2 resemble the high- T_N pnictides. Our magnetic susceptibility data hinted at a high (above our room temperature capabilities) T_N antiferromagnet, though the lack of unindexed NPD peaks refutes the presence of any long-range ordering above 160 K.

V. CONCLUSION

KCuMnS_2 and KLiMnS_2 were prepared through high-temperature reaction from the respective K and Li carbonates with pure metals under a CS_2 in Ar flow. Single crystals of KCuMnS_2 were prepared via a melt of the unwashed powder in an evacuated ampule. From neutron-diffraction data, we have proposed a striped pattern magnetic structure, as well as a noncollinear magnetic structure for KCuMnS_2 , with alternating layers oriented antiferromagnetically with a T_N of 160.5 K. Both structures have their magnetic moment oriented along only the ab plane and a moment that was refined to $0.92(2) \mu_B/\text{Mn}^{2+}$. We have also shown that by substituting Li^+ for Cu^+ , long-range ordering of the magnetic moment is destroyed. A feature of the KLiMnS_2 NPD pattern could indicate some short-range ordering, though it is not definitive as it could also be the result of inelastic scattering.

The magnetic susceptibility of KCuMnS_2 decreases with temperature, showing only a small feature near 160 K, until developing a Curie tail near 40 K. Single-crystal and pressed-pellet powder samples of KCuMnS_2 show primarily semiconducting behavior for resistivity/resistance measurements, respectively, except around the T_N of 160.5 K. Immediately below 160 K, KCuMnS_2 shows metallic behavior until resuming semiconducting behavior when the moment saturates, indicating that long-range magnetic order aids in the conductivity of the sample. Band structure calculations show that the Fermi level at the edge of the valence band for both compounds would make them susceptible to hole doping.

ACKNOWLEDGMENTS

Research at the University of Maryland was supported by the NSF Career Grant No. DMR-1455118, the Department of Commerce under the NIST Award No. 70NANB12H238, and the Air Force Office of Scientific Research through Grant No. FA9550-14-1-0332. The identification of any commercial product or trade name does not imply endorsement or recommendation by the National Institute of Standards and Technology. The authors acknowledge the University of Maryland supercomputing resources (<http://www.it.umd.edu/hpcc>) made available for conducting the research reported in this paper. The part of the research that was conducted at ORNL's High Flux Isotope Reactor was sponsored by the Scientific User Facilities Division, Office of Basic Energy Sciences, US Department of Energy.

- [1] R. Hoffmann and C. Zheng, *J. Phys. Chem.* **89**, 4175 (1985).
- [2] R. Hoffmann, *Angew. Chem., Int. Ed. Engl.* **26**, 846 (1987).
- [3] S. A. J. Kimber, A. Kreyssig, Y.-Z. Zhang, H. O. Jeschke, R. Valenti, F. Yokaichiya, E. Colombier, J. Yan, T. C. Hansen, T. Chatterji, R. J. McQueeney, P. C. Canfield, A. I. Goldman, and D. N. Argyriou, *Nat. Mater.* **8**, 471 (2009).
- [4] S. Peschke, T. Stürzer, and D. Johrendt, *Z. Anorg. Allg. Chem.* **640**, 830 (2014).
- [5] M. V. Sadovskii, E. Z. Kuchinskii, and I. A. Nekrasov, *J. Magn. Mater.* **324**, 3481 (2012).
- [6] R. Mittal, S. K. Mishra, S. L. Chaplot, S. V. Ovsyannikov, E. Greenberg, D. M. Trots, L. Dubrovinsky, Y. Su, T. Brueckel, S. Matsuishi, H. Hosono, and G. Garbarino, *Phys. Rev. B* **83**, 054503 (2011).
- [7] D. P. Shoemaker, D. Y. Chung, H. Claus, M. C. Francisco, S. Avci, A. Llobet, and M. G. Kanatzidis, *Phys. Rev. B* **86**, 184511 (2012).
- [8] D. Yuan, N. Liu, K. Li, S. Jin, J. Guo, and X. Chen, *Inorg. Chem.* **56**, 13187 (2017).
- [9] I. A. Nekrasov and M. V. Sadovskii, *JETP Lett.* **99**, 598 (2014).
- [10] D. C. Johnston, *Adv. Phys.* **59**, 803 (2010).
- [11] J. Paglione and R. L. Greene, *Nat. Phys.* **6**, 645 (2010).
- [12] Y. Mizuguchi and Y. Takano, *J. Phys. Soc. Jpn.* **79**, 102001 (2010).
- [13] X. H. Niu, S. D. Chen, J. Jiang, Z. R. Ye, T. L. Yu, D. F. Xu, M. Xu, Y. Feng, Y. J. Yan, B. P. Xie, J. Zhao, D. C. Gu, L. L. Sun, Q. Mao, H. Wang, M. Fang, C. J. Zhang, J. P. Hu, Z. Sun, and D. L. Feng, *Phys. Rev. B* **93**, 054516 (2016).
- [14] Q. Si, R. Yu, and E. Abrahams, *Nat. Rev. Mater.* **1**, 16017 (2016).
- [15] A. Newmark, G. Huan, M. Greenblatt, and M. Croft, *Solid State Commun.* **71**, 1025 (1989).
- [16] G. Huan, M. Greenblatt, and K. Ramanujachary, *Solid State Commun.* **71**, 221 (1989).
- [17] J. Yang, B. Chen, H. Wang, Q. Mao, M. Imai, K. Yoshimura, and M. Fang, *Phys. Rev. B* **88**, 064406 (2013).
- [18] R. Lizárraga, S. Ronneteg, R. Berger, A. Bergman, P. Mohn, O. Eriksson and L. Nordström, *Phys. Rev. B* **70**, 024407 (2004).
- [19] J. An, A. S. Sefat, D. J. Singh, and M.-H. Du, *Phys. Rev. B* **79**, 075120 (2009).
- [20] Y. Singh, M. A. Green, Q. Huang, A. Kreyssig, R. J. McQueeney, D. C. Johnston, and A. I. Goldman, *Phys. Rev. B* **80**, 100403(R) (2009).
- [21] D. C. Johnston, R. J. McQueeney, B. Lake, A. Honecker, M. E. Zhitomirsky, R. Nath, Y. Furukawa, V. P. Antropov, and Y. Singh, *Phys. Rev. B* **84**, 094445 (2011).
- [22] X. Lai, S. Jin, X. Chen, T. Zhou, T. Ying, H. Zhang, and S. Shen, *Mater. Express* **4**, 343 (2014).
- [23] M. Oledzka, C. Lee, K. Ramanujachary, and M. Greenblatt, *Mater. Res. Bull.* **32**, 889 (1997).
- [24] M. Oledzka, K. Ramanujachary, and M. Greenblatt, *Mater. Res. Bull.* **33**, 855 (1998).
- [25] M. Oledzka, K. V. Ramanujachary, and M. Greenblatt, *Mater. Res. Bull.* **31**, 1491 (1996).
- [26] M. Oledzka, J.-G. Lee, K. Ramanujachary, and M. Greenblatt, *J. Solid State Chem.* **127**, 151 (1996).
- [27] M. Oledzka, K. V. Ramanujachary, and M. Greenblatt, *Chem. Mater.* **10**, 322 (1998).
- [28] D. Schmitz and W. Bronger, *Z. Anorg. Allg. Chem.* **553**, 248 (1987).
- [29] W. Bronger, H. Hardtdegen, M. Kanert, P. Müller, and D. Schmitz, *Z. Anorg. Allg. Chem.* **622**, 313 (1996).
- [30] J. Lynn, Y. Chen, S. Chang, Y. Zhao, S. Chi, W. Ratcliff II, B. Ueland, and R. Erwin, *J. Res. Natl. Inst. Stand. Technol.* **117**, 60 (2012).
- [31] B. J. Campbell, H. T. Stokes, D. E. Tanner, and D. M. Hatch, *J. Appl. Crystallogr.* **39**, 607 (2006).
- [32] R. W. Cheary and A. Coelho, *J. Appl. Crystallogr.* **25**, 109 (1992).
- [33] G. M. Sheldrick, *Acta Crystallogr. Sect. C* **71**, 3 (2015).
- [34] P. Hohenberg and W. Kohn, *Phys. Rev.* **136**, B864 (1964).
- [35] W. Kohn and L. J. Sham, *Phys. Rev.* **137**, A1697 (1965).
- [36] G. Kresse and J. Furthmüller, *Phys. Rev. B* **54**, 11169 (1996).
- [37] G. Kresse and J. Furthmüller, *Comput. Mater. Sci.* **6**, 15 (1996).
- [38] G. Kresse and J. Hafner, *Phys. Rev. B* **47**, 558 (1993).
- [39] G. Kresse and J. Hafner, *Phys. Rev. B* **48**, 13115 (1993).
- [40] P. E. Blöchl, *Phys. Rev. B* **50**, 17953 (1994).
- [41] J. P. Perdew, K. Burke, and M. Ernzerhof, *Phys. Rev. Lett.* **77**, 3865 (1996).
- [42] H. J. Monkhorst and J. D. Pack, *Phys. Rev. B* **13**, 5188 (1976).
- [43] See Supplemental Material at <http://link.aps.org/supplemental/10.1103/PhysRevMaterials.3.044411> for the temperature dependence of lattice parameters for KCuMnS_2 , and additional DFT calculations.
- [44] P. Das, N. S. Sangeetha, A. Pandey, Z. A. Benson, T. W. Heitmann, D. C. Johnston, A. I. Goldman, and A. Kreyssig, *J. Phys.: Condens. Matter* **29**, 035802 (2017).
- [45] S. L. Brock, J. Greedan, and S. M. Kauzlarich, *J. Solid State Chem.* **113**, 303 (1994).
- [46] S. L. Brock, J. Greedan, and S. M. Kauzlarich, *J. Solid State Chem.* **109**, 416 (1994).
- [47] N. S. Sangeetha, A. Pandey, Z. A. Benson, and D. C. Johnston, *Phys. Rev. B* **94**, 094417 (2016).
- [48] L. Corliss, N. Elliott, and J. Hastings, *Phys. Rev.* **104**, 924 (1956).
- [49] R. Tappero, P. Wolfers, and A. Lichanot, *Chem. Phys. Lett.* **335**, 449 (2001).
- [50] C. G. Shull, W. A. Strauser, and E. O. Wollan, *Phys. Rev.* **83**, 333 (1951).
- [51] W. L. Roth, *Phys. Rev.* **110**, 1333 (1958).
- [52] J. M. Hastings, N. Elliott, and L. M. Corliss, *Phys. Rev.* **115**, 13 (1959).
- [53] R. D. Shannon and C. T. Prewitt, *Acta Crystallogr. Sect. B* **25**, 925 (1969).
- [54] E. E. Rodriguez, P. Zavalij, P. Hsieh, and M. A. Green, *J. Am. Chem. Soc.* **132**, 10006 (2010).
- [55] P. Zajdel, P. Hsieh, E. E. Rodriguez, N. P. Butch, J. D. Magill, J. Paglione, P. Zavalij, M. R. Suchomel, and M. A. Green, *J. Am. Chem. Soc.* **132**, 13000 (2010).
- [56] E. E. Rodriguez, C. Stock, P. Zajdel, K. L. Krycka, C. F. Majkrzak, P. Zavalij, and M. A. Green, *Phys. Rev. B* **84**, 064403 (2011).
- [57] C. Stock, E. E. Rodriguez, M. A. Green, P. Zavalij, and J. A. Rodriguez-Rivera, *Phys. Rev. B* **84**, 045124 (2011).
- [58] E. E. Rodriguez, D. A. Sokolov, C. Stock, M. A. Green, O. Sobolev, J. A. Rodriguez-Rivera, H. Cao, and A. Daoud-Aladine, *Phys. Rev. B* **88**, 165110 (2013).
- [59] C. Stock, E. E. Rodriguez, O. Sobolev, J. A. Rodriguez-Rivera, R. A. Ewings, J. W. Taylor, A. D. Christianson, and M. A. Green, *Phys. Rev. B* **90**, 121113(R) (2014).

- [60] X. Zhou, B. Wilfong, H. Vivanco, J. Paglione, C. M. Brown, and E. E. Rodriguez, *J. Am. Chem. Soc.* **138**, 16432 (2016).
- [61] E. E. Rodriguez, C. Stock, K. L. Krycka, C. F. Majkrzak, P. Zajdel, K. Kirshenbaum, N. P. Butch, S. R. Saha, J. Paglione, and M. A. Green, *Phys. Rev. B* **83**, 134438 (2011).
- [62] J. Zhao, Q. Huang, C. de la Cruz, S. Li, J. W. Lynn, Y. Chen, M. A. Green, G. F. Chen, G. Li, Z. Li, J. L. Luo, N. L. Wang, and P. Dai, *Nat. Mater.* **7**, 953 (2008).
- [63] C. Liu, T. Kondo, N. Ni, A. D. Palczewski, A. Bostwick, G. D. Samolyuk, R. Khasanov, M. Shi, E. Rotenberg, S. L. Bud'ko, P. C. Canfield, and A. Kaminski, *Phys. Rev. Lett.* **102**, 167004 (2009).
- [64] M. Rotter, M. Pangerl, M. Tegel, and D. Johrendt, *Angew. Chem. Intl. Ed.* **47**, 7949 (2008).
- [65] D. Johrendt and R. Pöttgen, *Phys. C: Superconductivity* **469**, 332 (2009).
- [66] J. Wu, J. Lin, X. Wang, Q. Liu, J. Zhu, Y. Xiao, P. Chow, and C. Jin, *Proc. Natl. Acad. Sci.* **110**, 17263 (2013).
- [67] E. E. McCabe, C. Stock, E. E. Rodriguez, A. S. Wills, J. W. Taylor, and J. S. O. Evans, *Phys. Rev. B* **89**, 100402(R) (2014).
- [68] Y. Singh, A. Ellern, and D. C. Johnston, *Phys. Rev. B* **79**, 094519 (2009).
- [69] M. Ramazanoglu, A. Sapkota, A. Pandey, J. Lamsal, D. Abernathy, J. Niedziela, M. Stone, R. Salci, D. Acar, F. Oztirpan, S. Ozonder, A. Kreyssig, A. Goldman, D. Johnston, and R. McQueeney, *Phys. B: Condens. Matter* **551**, 51 (2018).
- [70] A. Pandey, R. S. Dhaka, J. Lamsal, Y. Lee, V. K. Anand, A. Kreyssig, T. W. Heitmann, R. J. McQueeney, A. I. Goldman, B. N. Harmon, A. Kaminski, and D. C. Johnston, *Phys. Rev. Lett.* **108**, 087005 (2012).
- [71] D. E. McNally, J. W. Simonson, J. J. Kistner-Morris, G. J. Smith, J. E. Hassinger, L. DeBeer-Schmitt, A. I. Kolesnikov, I. A. Zaliznyak, and M. C. Aronson, *Phys. Rev. B* **91**, 180407(R) (2015).
- [72] Q. D. Gibson, H. Wu, T. Liang, M. N. Ali, N. P. Ong, Q. Huang, and R. J. Cava, *Phys. Rev. B* **91**, 085128 (2015).
- [73] W. Ratcliff II, A. Lima Sharma, A. Gomes, J. Gonzalez, Q. Huang, and J. Singleton, *J. Magn. Magn. Mater.* **321**, 2612 (2009).
- [74] C. Bridges, V. Krishnamurthy, S. Poulton, M. Paranthaman, B. Sales, C. Myers, and S. Bobev, *J. Magn. Magn. Mater.* **321**, 3653 (2009).